Amplified and directional spontaneous emission from arbitrary composite bodies: A self-consistent treatment of Purcell effect below threshold

Weiliang Jin,[1] Chinmay Khandekar,[1] Adi Pick,[2] Athanasios G. Polimeridis,[3] and Alejandro W. Rodriguez[1]
[1]*Department of Electrical Engineering, Princeton University, Princeton, New Jersey 08544, USA*
[2]*Department of Physics, Harvard University, Cambridge, Massachusetts 02138, USA*
[3]*Skolkovo Institute of Science and Technology, Moscow, Russia*
(Received 19 October 2015; revised manuscript received 22 December 2015; published 9 March 2016)

We study amplified spontaneous emission (ASE) from wavelength-scale composite bodies—complicated arrangements of active and passive media—demonstrating highly directional and tunable radiation patterns, depending strongly on pump conditions, materials, and object shapes. For instance, we show that under large enough gain, $\mathcal{PT}$ symmetric dielectric spheres radiate mostly along either active or passive regions, depending on the gain distribution. Our predictions are based on a recently proposed fluctuating-volume-current formulation of electromagnetic radiation that can handle inhomogeneities in the dielectric and fluctuation statistics of active media, e.g., arising from the presence of nonuniform pump or material properties, which we exploit to demonstrate an approach to modeling ASE in regimes where Purcell effect (PE) has a significant impact on the gain, leading to spatial dispersion and/or changes in power requirements. The nonlinear feedback of PE on the active medium, captured by the Maxwell-Bloch equations but often ignored in linear formulations of ASE, is introduced into our linear framework by a self-consistent renormalization of the (dressed) gain parameters, requiring the solution of a large system of nonlinear equations involving many *linear* scattering calculations.

DOI: 10.1103/PhysRevB.93.125415

I. INTRODUCTION

Noise in structures comprising passive and active materials can lead to important radiative effects [1], e.g., spontaneous emission (SE) [2], superluminescence [3], and fluorescence [4]. Although large-etalon gain amplifiers and related devices have been studied for decades [5–8], there is increased interest in the design of wavelength-scale composites for tunable sources of scattering and incoherent emission [9,10], or for realizing perfect absorbers [11] at midinfrared and visible wavelengths.

In this paper, we extend a recently developed fluctuating volume-current (FVC) formulation of electromagnetic (EM) fluctuations [12–15] to the problem of modeling spontaneous emission and scattering from composite, wavelength-scale structures, e.g., metal-dielectric spasers [16–18], subject to inhomogeneities in both material and noise properties. We begin by studying amplified spontaneous emission (ASE) from piecewise-constant composite bodies, showing that their emissivity can exhibit a high degree of directionality, depending sensitively on the gain profile and shape of the objects. For instance, we find that under large enough gain, the directivity of parity-time ($\mathcal{PT}$) symmetric spheres can be designed to lie primarily along active or passive regions, depending on the presence or absence of centrosymmetry, respectively. Such composite micron-scale emitters act as tunable sources of incoherent radiation, forming a special class of infrared/visible antennas exhibiting polarization- and direction-sensitive absorption and emission properties. An important ingredient for the design of directional emission is the ability to tune the gain profile of the objects, which can be far from homogeneous in realistic settings. Here, we consider two important sources of inhomogeneities affecting population inversion of atomically doped media: inhomogeneous pump profiles and modifications stemming from changes to the emitters' local radiative environment. Below threshold, the latter stems primarily from changes to atomic decay rates, which can be either enhanced or suppressed through the Purcell effect (PE) [19]. Because PE is sensitive to the gain and geometry of the objects, such a dependence manifests as a nonlinear and nonlocal interaction (or feedback) between the atomic medium and the optical environment [20], which we model within the stationary-phase approximation [21] via a self-consistent renormalization of the (dressed) atomic parameters. We show that this leads to a system of nonlinear equations, involving as many degrees of freedom as there are volumetric unknowns, which in principle require many scattering problems (radiation from dipoles) to be solved simultaneously, but which thanks to the low-rank nature of volume-integral equation (VIE) scattering operators [14] can be accurately obtained with far fewer scattering calculations than there are unknowns. Our predictions indicate that under significant PE, composite objects can exhibit a high degree of dielectric gain enhancement/suppression and inhomogeneity, affecting power requirements and emission patterns.

Gain-composite structures are the subject of recent theoretical and experimental work [1], and have been studied in a variety of different contexts, including spasers (combinations of metallic and gain media) with low-threshold characteristics [16–18,22,23], random structures with special absorption properties [24–28], and nanoscale particles with highly tunable emission and scattering properties [29,30]. $\mathcal{PT}$-symmetric structures have received special attention recently as they shed insights into important non-Hermitian physics, such as design criteria for realizing exceptional points [31], symmetry breaking [31], unidirectional scattering [32–34], and lasing thresholds [35]. Until recently, most studies of radiation/scattering from $\mathcal{PT}$ structures remained confined to 1D and 2D geometries [9,33,34,36–40]. In such low-dimensional systems, it is common to employ scattering matrix formulations [33,36,37] to solve for the complex eigenmodes

 ©2016 American Physical Society

and scattering properties of bodies, leading to many analytical insights. For instance, while the introduction of gain violates energy conservation, a generalized optical theorem can be obtained in 1D, establishing conditions for unidirectional transmission of light [32–34]. Other studies focus on 2D high-symmetry objects such as cylindrical or spherical bodies [38,39] or particle lattices [40], demonstrating strong asymmetric and gain-dependent scattering cross sections, while 3D structures such as ring resonators have been studied within the framework of coupled-mode theory [41,42]. With few exceptions [9], however, most studies of gain-composite bodies have focused on their scattering rather than emission properties.

Furthermore, while these systems are typically studied under the assumption of piecewise-constant [9,33,36] or linearly varying [10] gain profiles, in realistic situations, inhomogeneities in the pump or material parameters (e.g., arising from PE [20], hole burning [43,44], and gain saturation [44]) result in spatially varying dielectric profiles which alter SE. For example, the highly localized nature of plasmonic resonances in spasers results in strongly inhomogeneous pumping rates [17] and orders-of-magnitude enhancements in atomic radiative decay rates [45]. In random lasers [24], partial pumping plays an important role in determining the lasing threshold [26,46] and directionality [27,28]. Rigorous descriptions of lasing effects in these systems commonly resort to solution of the full Maxwell-Bloch (MB) equations, in which the electric field $\mathbf{E}$ and induced (atomic) polarization field $\mathbf{P}$ couple to affect the atomic population decay rates [47]. However, the MB equations are a set of coupled, time-dependent, nonlinear partial differential equations [48] which, not surprisingly, prove challenging to solve except in simple situations involving high-symmetry [45,49] or low-dimensional structures [1]. Despite their overhead, brute-force FDTD methods have been employed to study the transition from ASE to lasing in 1D random media [25,50], 2D metamaterials [49,51], photonic crystals [52], and, more recently, nanospasers [45].

A more recent, general-purpose method that is applicable to arbitrary structures is the steady-state *ab initio* laser theory (SALT), an eigenmode formulation that exploits the stationary-inversion approximation to remove the time dependence and internal atomic dynamics of the MB equations [21,53,54], yet captures important nonlinear effects such as hole burning and gain saturation [21] through effective two-level polarization and population equations [55]. The resulting nonlinear eigenvalue equation can be solved via a combination of Newton-Raphson [48,56], sparse-matrix solver [57], and nonlinear eigenproblem [58] techniques, exploiting either spectral "CF" basis expansions (especially suited for structures with special symmetries) [59] or brute-force methods [60] that can handle a wider range of shapes and conditions. Although this formulation can describe many situations of interest, it nevertheless poses computational challenges in 3D or when applied to structures supporting a large number of modes [48]. Furthermore, the impact of noise below or near threshold has yet to be addressed, though recent progress is being made along these directions [48,56].

Below and near the lasing threshold, stimulated emission is often negligible, enabling linearized descriptions of the gain medium [44,47,61,62]. Such approximations, however, ignore nonlinearities stemming from the induced radiation rate $\sim\mathbf{E}\cdot\mathbf{P}$ present in the MB equations, which captures feedback on the atomic medium due to amplification or suppression of noise from changes in the local density of states (also known as Purcell effect) [45,63,64]. Here, we show that PE can be introduced into the linearized framework via a self-consistent renormalization or dressing of the gain parameters, an approach that was recently suggested [20] but which has yet to be demonstrated. In particular, working within the scope of the linearized MB equations and stationary-inversion approximation, we capture the nonlinear feedback of ASE on gain, i.e., the steady-state enhancement/suppression of gain and atomic decay rates due to PE, via a series of nonlinear equations involving many coupled, *linear*, classical scattering calculations—local density of states or far-field emission due to electric dipole currents. Since the gain profile can become highly spatially inhomogeneous, it is advantageous to tackle this problem using brute-force methods, e.g., finite differences [65], finite elements [66], or via the scattering VIE framework described below. Our FVC method is particularly advantageous in that it is general and especially suited for handling scattering problems with large numbers of degrees of freedom (defined only within the volumes of the objects), in contrast to eigenmode expansions [59] which become inefficient in situations involving many resonances [48,59] or near-field effects [67,68].

II. FORMULATION

Active medium. To begin with, we review the linearized description of a gain medium consisting of optically pumped four-level atoms, as shown in Fig. 1: a dense collection of active emitters (e.g., dye molecules [44] or quantum dots [69,70]) embedded in a passive (background) dielectric medium ϵ_r. (Note that our choice of four-level system here is merely illustrative since the same approach described below also applies to other active media.) Below threshold where stimulated emission (and effects such as hole burning) can be safely ignored [44], the effective permittivity of such a medium can be well approximated by a simple two-level Lorentzian gain profile [44,61,62],

$$\epsilon(\omega,\mathbf{x}) = \epsilon_r(\omega) + \underbrace{\frac{4\pi g(\mathbf{x})^2}{\hbar\gamma_\perp}\frac{\gamma_\perp D_0(\mathbf{x})}{\omega-\omega_{21}+i\gamma_\perp}}_{\epsilon_g(\mathbf{x},\omega)}, \qquad (1)$$

where ϵ_g depends explicitly on the frequency ω_{12}, polarization decay rate $\gamma_\perp$ (or gain bandwidth), coupling strength $g^2 = \frac{3\hbar c^3}{2\sqrt{\epsilon_r}\omega_{21}^3}\gamma_{21}^r$ [61,62], and inversion factor $D_0 = n_2 - n_1$ associated with the $2 \to 1$ transition. Under the adiabatic or stationary-inversion approximation [21] and assuming that the system is pumped at ω_{30}, the steady-state population inversion is given by:

$$D_0 = \frac{\left(1-\frac{\gamma_{21}}{\gamma_{10}}\right)\mathcal{P}/\gamma_{21}}{1+\left(A\frac{\gamma_{21}}{\gamma_{32}}+\frac{\gamma_{21}}{\gamma_{10}}+1\right)\mathcal{P}/\gamma_{21}}n. \qquad (2)$$

(Note that in a dense medium, $\gamma_\perp \gg \gamma_{21}$ is dominated by collisional and dephasing effects [44].) Here, $A = 1(2)$ for

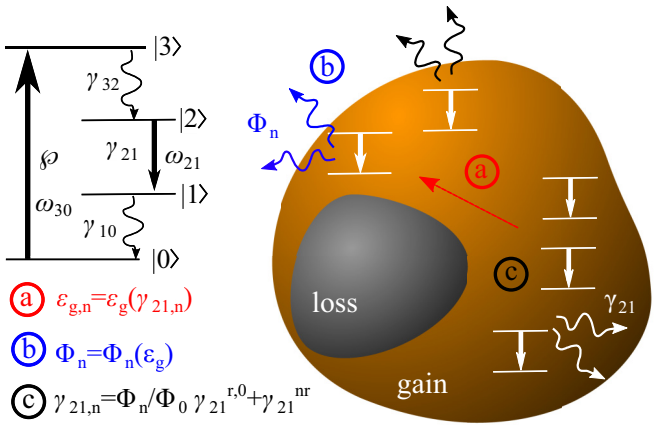

FIG. 1. Schematic of a gain-loss composite body consisting of a dense (active) collection of four-level atoms (left inset) optically pumped via monochromatic light at frequency ω_{30} and pump rate $\mathcal{P}$, resulting in population inversion and spontaneous emission (SE) at ω_{21}. The nonlinear feedback of Purcell effect on the SE rate of the object is captured via a system of nonlinear equations illustrated on the right schematic, in which (a) the dielectric constant at the location of the nth emitter depends on the corresponding atomic decay rate $\gamma_{21,n}$ through (1), (b) the radiative emission Φ_n of a classical dipole at the location of the nth emitter, described by (7), is altered, e.g. enhanced or suppressed, by the surrounding $\varepsilon(\mathbf{x})$, and (c) the radiative decay rate $\gamma^{\mathrm{r}}_{21,n}$ of the emitter is dressed by the Purcell effect through (8), which in turn affects the dielectric response in (1).

incoherent (coherent) pump source; c denotes the speed of light, n_i the population (per unit volume) of level i, $n = \sum_i n_i$ the overall atomic population, $\gamma_{ij} = \gamma^r_{ij} + \gamma^{nr}_{ij}$ the decay rate from level $i \to j$, consisting of radiative and nonradiative terms, respectively, and $\mathcal{P}(\mathbf{x}) = \frac{\sigma c}{\sqrt{\epsilon_r(\omega_{30})}\hbar\omega_{30}}|E(\mathbf{x},\omega_{30})|^2$ is the position-dependent pump rate from $0 \to 3$, which is often the main source of spatial dispersion.

The SE properties of such a medium are described by the fluctuation-dissipation theorem (FDT) [71–73]. In particular, local thermodynamic considerations imply that the presence of absorption or amplification must be accompanied by fluctuating polarization currents σ whose correlation functions, $\langle \sigma_i(\mathbf{x},\omega)\sigma^*_j(\mathbf{y},\omega)\rangle = \frac{4}{\pi}\operatorname{Im}\epsilon_g(\mathbf{x},\omega)n_2/(n_1 - n_2)\delta(\mathbf{x}-\mathbf{y})\delta_{ij}$, depend on the corresponding macroscopic gain profile $\operatorname{Im}\epsilon_g$ and population inversion, $n_2/(n_1 - n_2)$ [74]. The latter is often described in terms of an effective (local) temperature T defined with respect to the Planck spectrum [71], $(e^{\hbar\omega/k_BT} - 1)^{-1}$, whose value turns negative [75] for systems undergoing population inversion, $n_2 > n_1$, where $T \to 0^-$ in the limit of complete inversion and $T \to -\infty$ when the system is in the ground state [72]. In the particular case of a steady-state four-level system, the relative populations n_2/n_1 depend only on the relative decay rates and one finds that $k_BT = \hbar\omega\ \ln(\frac{n_1}{n_2}) = \hbar\omega\ \ln(\frac{\gamma_{10}}{\gamma_{21}})$ depends implicitly on the pumping rate only through changes in the atomic decay rates (Purcell effect); in contrast, the effective temperature of three-level systems depends explicitly on the pumping rate. The presence of inhomogeneities in the dielectric function and fluctuation statistics can be a hurdle for calculations of SE that rely on scattering-matrix formulations [76,77], but here we exploit a recently developed FVC formulation based on the VIE method which captures all of the relevant physics.

FVC formulation. In order to obtain the individual and/or cumulative radiation from all dipoles within a given object, we exploit the FVC formulation introduced in [14] and summarized here. The starting point of FVC is the VIE formulation of EM scattering [66], describing scattering of an incident, six-component electric ($\mathbf{E}$) and magnetic ($\mathbf{M}$) field $\phi_{\mathrm{inc}} = (\mathbf{E};\mathbf{H})$ from a body described by a spatially varying 6×6 susceptibility tensor $\chi(\mathbf{x})$. Given a six-component electric ($\mathbf{J}$) and magnetic ($\mathbf{M}$) dipole source $\sigma = (\mathbf{J};\mathbf{M})$, the incident field is obtained via a convolution ($\star$) with the 6×6 homogeneous electric and magnetic Green's function (GF) of the ambient medium $\Gamma(\mathbf{x},\mathbf{y})$, such that $\phi_{\mathrm{inc}} = \Gamma \star \sigma = \int d^3\,\mathbf{y}\Gamma(\mathbf{x},\mathbf{y})\sigma(\mathbf{y})$. Exploiting the volume equivalence principle [66], the unknown scattered fields $\phi_{\mathrm{sca}} = \Gamma \star \xi$ can also be expressed via convolutions with Γ, except that here $\xi = -i\omega\chi\phi$ are the (unknown) bound currents in the body, related to the total field inside the body $\phi = \phi_{\mathrm{inc}} + \phi_{\mathrm{sca}}$ through χ. Writing Maxwell's equations in terms of the bound currents, we arrive at the so-called JM-VIE equation [12]:

$$\underbrace{[\Gamma \star + (i\omega\chi)^{-1}]}_{Z}\,\xi = -(\Gamma \star \sigma), \tag{3}$$

whose solution can be obtained by a Galerkin discretization of the currents $\sigma(\mathbf{x}) = \sum_n s_n b_n(\mathbf{x})$ and $\xi(\mathbf{x}) = \sum_n x_n b_n(\mathbf{x})$ in a convenient, orthonormal basis $\{b_n\}$ of N six-component vectors, with vector coefficients s and x, respectively. The resulting matrix expression can be written in the form $x + s = Ws$, defining the VIE matrix $(W^{-1})_{m,n} = \langle b_m, b_n + i\omega\chi(\Gamma \star b_n)\rangle$ with $\langle,\rangle$ denoting the standard conjugated inner product. Direct application of Poynting's theorem $\Phi = \frac{1}{2}\operatorname{Re}\int d^3\mathbf{x}\,(\mathbf{E}^* \times \mathbf{H})$ yields the following expression for the far-field radiation flux from σ (here, a single dipole source embedded within the volume) [78]:

$$\Phi_\sigma = -\tfrac{1}{2}\operatorname{Re}\xi^*\phi = -\tfrac{1}{2}\operatorname{Re}(\xi+\sigma)^*\Gamma\star(\xi+\sigma), \tag{4}$$

$$= -\tfrac{1}{2}(x+s)^*\operatorname{sym}G(x+s), \tag{5}$$

$$= -\tfrac{1}{2}s^*W^*\operatorname{sym}GWs, \tag{6}$$

$$= -\tfrac{1}{2}\operatorname{Tr}[DW^*\operatorname{sym}GW], \tag{7}$$

where $D = s^*s$ and G are $N\times N$ matrices, with $G_{mn} = \langle b_m, \Gamma\star b_n\rangle$.

If $\{b_n\}$ is chosen to be a localized basis of unit amplitude, i.e., $\langle b_m, b_n\rangle = \delta_{nm}$, volume elements, then the flux contribution from a given dipole source in the volume (including different polarizations) b_n is precisely the diagonal element $-\frac{1}{2}(W^*\operatorname{sym}GW)_{n,n}$. In contrast, the overall ASE is given by an ensemble average over all such fluctuating dipole sources $\Phi = \langle\Phi_\sigma\rangle$, in which case the elements of the matrix D, which encodes information about the current amplitudes, are given by the current-current correlations $\langle D\rangle_{mn} = \iint d^3\mathbf{x}\,d^3\mathbf{y}\,b^*_m(\mathbf{x})\langle\sigma(\mathbf{x})\sigma^*(\mathbf{y})\rangle b_n(\mathbf{y})$, determined by the FDT above. Direct computation of (7) is expensive due to the large dimensionality N of the problem, but it turns out that the Hermitian, negative-semidefinite, and low-rank nature of $\operatorname{sym}G$ (since it is associated with the smooth, imaginary part of the Green's functions) enables reexpressing the trace as the Frobenius norm of a low-rank matrix. Specifically,

decomposing sym $G = -U_r S_r U_r^*$ via a fast approximate SVD [79], where $r \ll N$ [80], and further decomposing $S_r = L_S L_S^*$, we find that the product W^* sym GW can be written in the form QQ^*, with $Q = W^* U_r L_S$, reducing the calculation of the diagonal elements to a small series $r \ll N$ of scattering calculations (matrix-inverse operations) [12]. Similarly, as shown in [14], the same follows for the overall ASE which is just a weighted sum of the diagonal elements. For example, while the calculations below require $N \geqslant 40^3$ basis functions to obtain accurate spatial resolution, we find that generally $r \lesssim 20$.

Purcell effect. Although often assumed to be uniform below threshold, the atomic radiative decay rates γ_{ij}^r entering (1) are in fact position dependent due to PE [45,63], leading to changes in the dipole coupling g and population inversion factor D_0, either enhancing or suppressing (quenching) gain [63]. In what follows, we only consider modifications to the radiative decay rate at the lasing transition γ_{21}^r; unlike the pump which is incident at a nonresonant frequency, changes in γ_{21}^r can have a significant impact on SE and must therefore be treated self-consistently.

The impact of PE on the radiative decay rate γ_{21}^r of an atom at some position b_n is captured by the coupling of the atomic polarization and electric fields $\sim \mathbf{P} \cdot \mathbf{E}$, or the induced radiation term in the MB equations, in the presence of the noise and surrounding dielectric environment [81]. While technically this requires abandoning the linear model above, the weak nature of noise (ignoring stimulated emission) implies that the latter can also be obtained (perturbatively) from a *linear*, classical calculation: the radiative flux Φ_{b_n} from a classical dipole at b_n. Specifically, the renormalized or dressed decay rate of an atom at position $\mathbf{x}$ can be expressed as [63]

$$\gamma_{21}^r(\mathbf{x}) = \mathcal{F}(\mathbf{x})\gamma_{21}^{r,0}, \tag{8}$$

where $\mathcal{F}(\mathbf{x})$ denotes the Purcell factor of a dipole at $\mathbf{x}$, and the superscript "0" denotes the decay rate of the atomic population in the lossy (background) medium. It follows that the decay rate associated with a given b_n and entering (1) is given by $\gamma_{21}(b_n) = \gamma_{21}^{nr} + \mathcal{F}_{b_n}\gamma_{21}^{r,0}$, where the Purcell factor

$$\mathcal{F}_{b_n} = \Phi_{b_n}/\Phi^0. \tag{9}$$

[Note that all $\Phi_{b_n} \sim (W^* \text{ sym } GW)_{n,n}$ can be computed very fast, as explained above, and that $\mathcal{F}_{b_n}$ does not depend on the amplitude of the fluctuations since it is measuring the relative radiation rate of a classical emitter at this position.] Here, we assume that the bulk (background) medium ϵ_r only has a significant impact on $\gamma_{21}^{nr,0}$ (obtained either experimentally or theoretically by accounting for atomic interactions within the bulk) [44] but not on the radiative decay rate $\gamma_{21}^{r,0}$, in which case $\Phi^0 = \omega^4/12\pi\epsilon_0 c^3$ is the emission rate of the atom in vacuum (assuming a unit-amplitude dipole). Note that in a lossy medium, e.g., in metals, the bare γ_{21}^0 will be dominated by nonradiative processes [82,83], leading to small quantum yields (QY) $\gamma_{21}^{r,0}/\gamma_{21}^0 \ll 1$. Technically, the calculation of the Purcell factor requires integration over the gain bandwidth, $\mathcal{F}_{b_n} = \int d\omega \frac{\gamma_\perp/\pi}{\gamma_\perp^2+(\omega-\omega_{21})^2} \frac{\Phi_{b_n}(\omega)}{\Phi^0(\omega)}$, but here we make the often-employed and simplifying assumption that $\gamma_\perp \gg \gamma_{21}$ and $\gamma_\perp \lesssim$ spectral radiative features [84,85], so as to only consider radiation at ω_{21}.

The gain profile of a body subject to an incident pump rate $\mathcal{P}$ can be obtained by enforcing that (1) and (8) be satisfied simultaneously. Such systems of nonlinear equations are most often solved iteratively using one or a combination of algorithms, ranging from simple fixed-point iteration [86] to more sophisticated approaches like Newton-Raphson and nonlinear Arnoldi methods [48,87]. Essentially, as illustrated in Fig. 1, starting with the bare parameters, dressed decay rates are computed via (8) from the radiation equation (7) after which, having updated the gain-medium equation (1), the entire process is repeated until one arrives at a fixed point of the system. In principle, this requires hundreds of thousands N of scattering calculations (flux from each dipole source in the active region) to be solved *per iteration*, which becomes prohibitive in large systems, but the key here is that the entire spatially varying flux $\{\Phi_{b_n}\}$ throughout the body can be computed extremely fast, requiring far fewer ($\ll N$) scattering calculations (as described above). Note that these large systems of nonlinear equations have many fixed points and hence convergence to the correct solution is never guaranteed, depending largely on the initial guess and algorithm employed [88]. However, a convenient and effective approach is to begin by first solving the system in the fast-converging (passive) regime $\mathcal{P}n/\gamma_{12} \ll 1$, and then employing this solution as an initial guess at larger pumps.

III. RESULTS

We begin this section by showing that wavelength-scale composite bodies can exhibit highly complex, tunable, and directional radiation patterns. Although it is not surprising that objects undergoing ASE (once known as "mirrorless lasers") exhibit highly directed radiation patterns [89], few studies have gone beyond large-etalon Fabry-Pérot cavities [90] or fiber waveguides [91], often modeled via ray-optical or scalar-wave equations [1], which miss important effects present in wavelength-scale systems [48]. Further below, we show that dielectric inhomogeneities arising from the pump and/or radiation process can also introduce important changes to the ASE patterns. In particular, we apply the renormalization approach described above to consider the *nonlinear* impact of Purcell effect on the gain medium, and show that while in many cases a homogeneous approximation leads to accurate results, there are situations where these can fail dramatically. These calculations serve only as a proof of principle and involve highly doped (Er^{3+} and rhodamine) dielectric objects, allowing faster computations but requiring very large values of Im ϵ_g to achieve significant gain. Similar results follow, however, in systems subject to smaller ϵ_g or smaller doping densities, at the expense of larger pump powers or by exploiting resonances with greater confinement or smaller radiative loss rates (e.g., compact bodies of larger dimensions and/or refractive indices, or more complex structures such as photonic-crystal resonators).

Tunable radiation patterns. We begin by exploring SE from piecewise-constant $\mathcal{PT}$-symmetric spheres (Fig. 2 insets) consisting of a background dielectric medium, e.g., nanocomposite polymers [92,93] or semiconductors [41,94], doped with active materials to realize different (N) regions of equal gain (orange) or loss (gray). Figure 2(a) shows the SE flux Φ

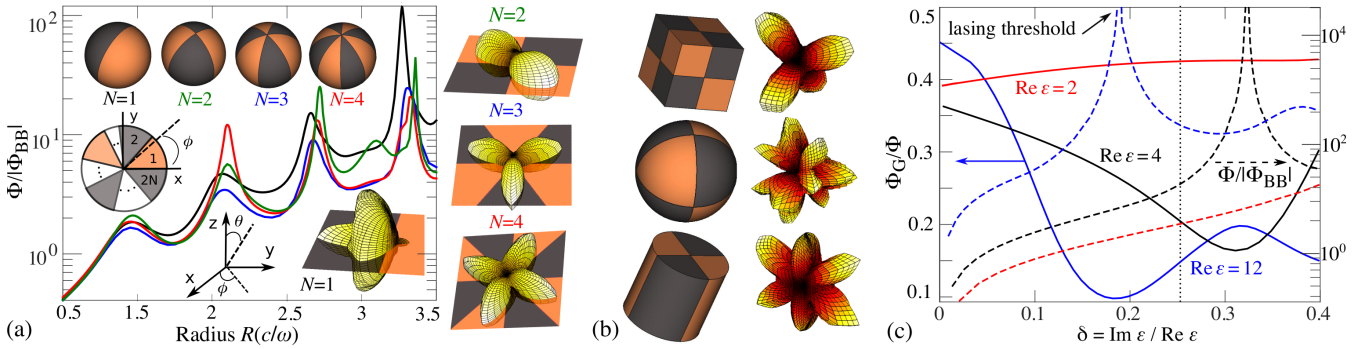

FIG. 2. (a) SE flux Φ from $\mathcal{PT}$-symmetric spheres consisting of $N = \{1,2,3,4\}$ (black, green, blue, and red lines) regions of equal gain (orange) and loss (gray), with permittivities $\epsilon = 4 \pm i$ and gain temperature $T \to 0^-$ K (corresponding to complete population inversion), as a function of sphere radius R (for a fixed vacuum wavelength $2\pi c/\omega$). $\Phi(\omega)$ is normalized by the flux $|\Phi_{BB}(\omega)| = R^2(\omega/c)^2\hbar\omega$ from a "blackbody" of the same surface area and temperature. Insets show angular radiation intensities $\Phi(\theta,\phi)$ for different N at selective radii $R = \{2.6,3,2.7,2.1\}(c/\omega)$ (corresponding to increasing N), with orange/gray colormaps denoting regions of gain/loss. (b) Selected $\Phi(\theta,\phi)$ of various $\mathcal{PT}$-symmetric shapes, including "beach balls," "magic" cubes, and cylinders, showing complex directivity patterns that depend strongly on the centrosymmetry of the objects. Here the color white (black) refers to the maximum (minimum) flux value. (c) Peak SE flux Φ (right axis, dashed lines) and directivity Φ_G/Φ (left axis, solid lines), or the ratio of the flux emitted along gain direction Φ_G (see text) to the total flux Φ, near the third resonance of the $N = 1$ sphere, as a function of the gain/loss tangent $\delta = |\operatorname{Im}\epsilon|/\operatorname{Re}\epsilon$ and for multiple values of $\operatorname{Re}\epsilon = \{2,4,12\}$ (red, black, and blue lines), where the vertical dashed black line denotes δ for (a). The plots show increased directivity attained as the system approaches the lasing threshold (marked in the case of $\operatorname{Re}\epsilon = 12$, where Φ diverges).

from spheres of varying $N = \{1,2,3,4\}$ (black, green, blue, red lines) and gain/loss permittivities $\epsilon = 4 \pm i$, at a fixed frequency ω and gain temperature $T \to 0^-$ K (corresponding to complete inversion), as a function of radius R (in units of the vacuum wavelength c/ω). $\Phi(\omega)$ is normalized by the flux $|\Phi_{BB}(\omega)| = R^2(\omega/c)^2\hbar\omega$ from a "blackbody" of the same surface area and temperature. As expected, Φ shows peaks at selected $R \gtrsim (c/\omega)$ corresponding to enhanced emission at Mie resonances. (Note that the amplitude of the peaks in Φ continue to increase with increasing R due to decreased radiative losses, with the bandwidth of the resonances narrowing as the system reaches the lasing transition, at which point our linear approach breaks down.) As spontaneous emission increases, so too does the directivity, illustrated by the radiation patterns $\Phi(\theta,\phi)$ shown on the insets of Fig. 2(a) at selected R, whose high directionality contrasts sharply with the emission profile of passive particles. (With few exceptions [15], the latter tend to emit quasi-isotropically, as can be verified by decreasing the gain of the spheres.) We find that the direction of largest ASE changes drastically with respect to N, with radiation coming primarily from either active or passive regions depending on whether the spheres exhibit or lack centrosymmetry, respectively (insets). In particular, the ratio Φ_G/Φ of the flux emitted from the gain surfaces,

$$\Phi_G = \sum_{k=0}^{N-1} \int d\theta \, \sin^2(\theta) \int_{2\pi k/N}^{\pi(2k+1)/N} d\phi \, \Phi(\theta,\phi),$$

to the total flux Φ, is generally $\lesssim 0.5$ for odd N (centrosymmetric) and $\gtrsim 0.5$ otherwise. For instance, near the peak of the third resonance at $R \approx 3(c/\omega)$, $N = 1(2)$ spheres exhibit $\Phi_G/\Phi \approx 0.1(0.75)$. The sensitive dependence of emission pattern on geometry and gain profile is not unique to spherical structures, as illustrated in Fig. 2(b), which shows $\Phi(\theta,\phi)$ for various shapes, including "magic" cubes, "beach balls," and cylinders—as before, the presence/absence of centrosymmetry results in high/low gain directivity.

To understand the features and origin of these emission patterns, Fig. 2(c) explores the dependence of the peak Φ (dashed lines) and Φ_G/Φ (solid lines) on the gain/loss tangent $\delta = |\operatorname{Im}\epsilon|/\operatorname{Re}\epsilon$ of the $N = 1$ sphere, near the third resonance and for multiple values of $\operatorname{Re}\epsilon = \{2,4,12\}$. As shown, there is negligible ASE in the limit $\operatorname{Im}\epsilon \to 0$, yet the localization of fluctuating dipoles to the gain-half of the (increasingly uniform) sphere leads to a small (though observable) amount of directionality, favoring emission toward the loss direction. The tendency of dipoles within a sphere to emit in a preferred direction has been studied in the context of fluorescence [95] in the ray-optical limit $R \gg c/\omega$, which as shown here is exacerbated in the presence of gain [96]: essentially, dipoles within a sphere tend to emit in the direction opposite the nearest surface, which explains why spheres having/lacking centrosymmetry tend to emit along directions of gain/loss. Moreover, in order to achieve large directivity, there needs to be a significant amount of mode confinement and gain, as illustrated by the negligible ASE and directivity of the $\operatorname{Re}\epsilon = 2$ sphere. Finally, we find that for large enough $\operatorname{Re}\epsilon$, the directivity increases with increasing $\operatorname{Im}\epsilon$, peaking at a critical δ, corresponding to the onset of lasing. Such a transition is marked by a diverging Φ near the threshold along with a corresponding narrowing of the resonance linewidth (not shown). (Note that our predictions close to and above this critical gain are no longer accurate since they neglect important effects stemming from stimulated emission [97]. For instance, at and above the critical gain, the resonance linewidth goes to zero and then broadens with increasing $\operatorname{Im}\epsilon$, while it is well known that nonlinear gain saturation results in a finite laser linewidth [53,54].) Nevertheless, our results demonstrate that a significant amount of directivity can be obtained below the onset of lasing, where the linear approximation is still valid.

Pump inhomogeneity. Next, we employ the four-level gain model of (1) to illustrate the impact of gain inhomogeneities on ASE. While both $\mathcal{P}$ and PE are simultaneous sources of spatial dispersion, for the sake of comparison we consider each independently of one another. We begin by studying the impact of pump on the $N = 2$ sphere (above) for an active region consisting of a background medium $\epsilon_r = 4$ that is doped with rhodamine 800 dye molecules with atomic parameters: $\omega_{21} = 2.65 \times 10^{15}\text{s}^{-1}$ ($\lambda \approx 711$ nm), $\gamma_\perp/\omega_{21} = 0.04$, $\gamma_{21}/\omega_{21} = 7.5 \times 10^{-7}$, $\gamma_{32}/\omega_{21} = \gamma_{10}/\omega_{21} = 10^{-3}$, QY of 20%, and concentration $n = 40$ mM (2.4×10^{19} cm^{-3}) [61]. Note that since $\omega_{30} \gg \omega_{21}$, it is safe to neglect feedback due to PE and hence $\mathcal{P}$ is determined from a single scattering calculation [14]. For these parameters [61], a pump rate $\mathcal{P}/\gamma_{21} \approx 3$ results in $-\text{Im}\,\epsilon_g(\omega_{21}) \approx 1$. We consider illumination with **z**-polarized plane waves incident from two opposite directions along the x-y plane, shown schematically in Fig. 3. The insets depict $z = 0$ cross sections of the resulting ϵ_g profile [Fig. 3(a)] at $R = 3.4(c/\omega_{21})$ along with emission patterns $\Phi(\theta,\phi)$ [Fig. 3(b)] at $R = 4(c/\omega_{21})$, under three incident conditions, corresponding to different directions of incidence, $\hat{\mathbf{x}}\cos\phi + \hat{\mathbf{y}}\sin\phi$ and $-\hat{\mathbf{x}}\cos\phi - \hat{\mathbf{y}}\sin\phi$, with $\phi = \{0, \pm\pi/4\}$; in each case, the incident power is chosen such that $\max\{-\text{Im}[\epsilon_g]\} = 1$. As shown, the gain profiles vary dramatically with respect to position and incident angle, with $\text{Im}\,\epsilon_g$ changing from $0 \to 1$ on the scale of the wavelength. These spatial variations lead to correspondingly large changes in the overall ASE [Fig. 3(a)] and directivity [Fig. 3(b)]. More importantly, we find that these features cannot be explained by naive, uniform-medium approximations (UMA). For instance, replacing ϵ_g with the average gain $\langle\epsilon_g\rangle = \frac{1}{V}\int_V \epsilon_g$ in the case $\phi = -\pi/4$, we find that UMA predicts an emission rate $\Phi/\Phi_{\text{BB}} \approx 30$ that is three times larger than that predicted by exact calculations. Differences in illumination angle also result in different angular radiation patterns $\Phi(\theta,\phi)$. For instance, we find that $\phi = -\pi/4$ leads to much more isotropic radiation than $\phi = \{0,\pi/4\}$, a consequence of the larger $\text{Im}\,\epsilon_g$ near the center of the sphere and the fact that dipoles near the center tend to radiate more isotropically and efficiently than those farther away.

Purcell effect. We now consider inhomogeneities arising from PE, assuming a uniform pump and doping concentration. In particular, we apply the self-consistent framework described in Sec. II to study ASE from the $N = 1$ sphere above, but with an active region consisting of a background medium $\epsilon_r = 4$ that is doped with Er^{3+} atoms [47,98], with parameters $\omega_{21} = 6.28 \times 10^{14}$ s^{-1} ($\lambda \approx 2.8$ μm), $\gamma_\perp/\omega_{21} = 0.03$, $\gamma_{21}/\omega_{21} = 5 \times 10^{-5}$, $\gamma_{32}/\omega_{21} = \gamma_{10}/\omega_{21} = 1$, bare QY of 50%, and concentration $n = 10^{19}$ cm^{-3}. (Further below we also consider a different geometry, a metal-dielectric spaser consisting of similar gain parameters but passive metallic regions.) Here, a pump rate $\mathcal{P}/\gamma_{21} = 10^{-4}$ results in $-\text{Im}\,\epsilon_g(\omega_{21}) \approx 1$ in the absence of PE. As discussed above, we employ fixed-point iteration to solve (7) and (8) and hence obtain consistent values of ϵ_g and Φ, starting with the bare ($\mathcal{F} = 1$) atomic parameters and iterating until the gain parameters converge to the nearest fixed point. Generally, the convergence rate of the fixed-point algorithm depends sensitively on the chosen parameter regime, requiring larger number of iterations with decreasing $\frac{\partial\epsilon_g}{\partial\gamma_{21}^r}$ (decreasing local slope) [86]. The convergence also depends on the degree of nonlinearity in the system, which in the case of our four-level system can be significant under small QY ($\gamma_{21}^r/\gamma_{21} \ll 1$), large $\mathcal{P}$, or $\gamma_{21}/\gamma_{10} \lesssim 1$ (in which case there is significant gain saturation). Nevertheless, in practice we find that for a wide range of parameters, a judicious combination of fixed-point iteration and Anderson acceleration [88] ensures convergence within dozens of iterations. The bottom/top insets of Fig. 4(c)

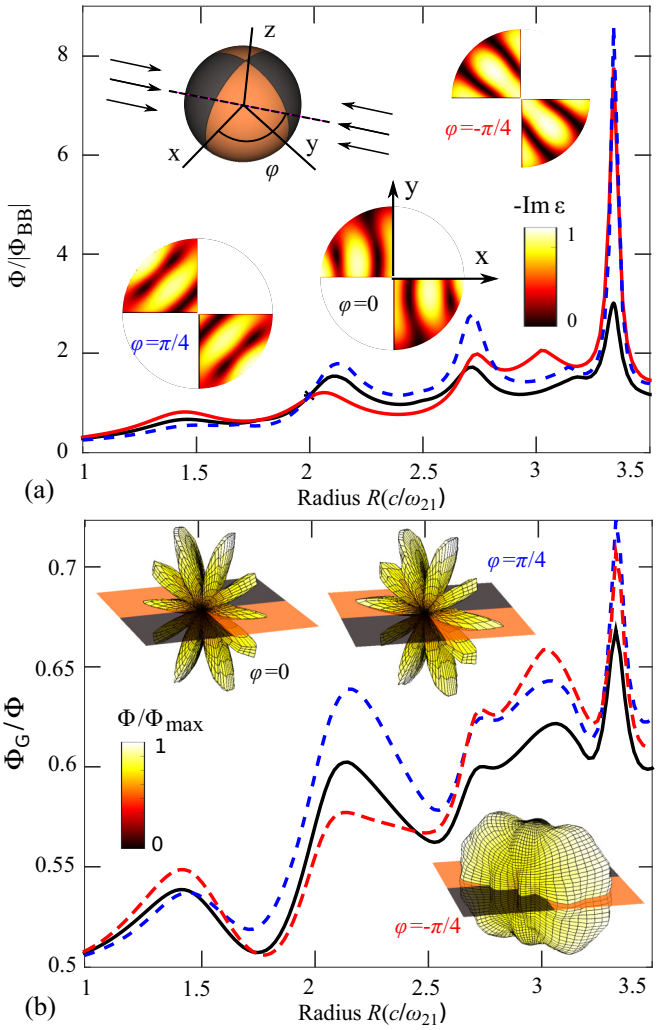

FIG. 3. (a) SE flux Φ and (b) gain directivity Φ_G/Φ, or the ratio of the flux emitted along the gain directions Φ_G (see text) to the total flux Φ, from the $N = 2$ sphere (inset) of Fig. 2 at frequency ω_{21}, corresponding to the transition frequency of an active region consisting of Rhodamine 800 dye molecules. The gain medium is excited by plane waves propagating in opposite directions, $\mathbf{x}\cos\phi + \mathbf{y}\sin\phi$ and $-\mathbf{x}\cos\phi - \mathbf{y}\sin\phi$, for three different orientations, $\phi = 0$ (black line), $\pi/4$ (blue line), and $-\pi/4$ (red line), leading to significant spatial inhomogeneities. Φ is normalized by Φ_{BB} as in Fig. 2 and plotted as a function of radius R, in units of the dye $2 \to 1$ transition wavelength c/ω_{21} (see text). Insets in (a) show $z = 0$ cross sections of the resulting gain profiles $-\text{Im}\epsilon_g$ at $R = 3.4(c/\omega_{21})$, while those in (b) show angular radiation intensities $\Phi(\theta,\phi)$ normalized by the maximum intensity Φ_{max} at $R = 4(c/\omega_{21})$ for the different pump orientations.

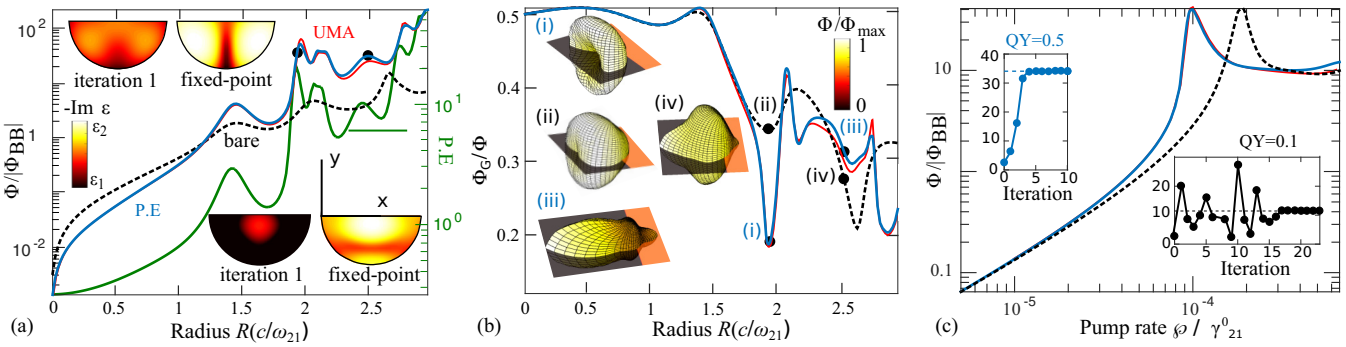

FIG. 4. Self-consistent treatment of Purcell effect (PE) based on solution of (1) and (8) using fixed-point iteration. (a) SE flux Φ normalized by $\Phi_{\rm BB}$ as in Fig. 2 and (b) gain directivity Φ_G/Φ from the $N = 1$ sphere of Fig. 2, as a function of radius R (in units of c/ω_{21}), with an active medium consisting of Er^{3+} atoms and subject to a uniform pump rate $\mathcal{P}/\gamma_{21}^0 = 10^{-4}$, where ω_{21} and γ_{21}^0 denote the bulk (bare) $2 \to 1$ transition frequency and decay rate of the atoms, respectively. Top/bottom insets in (a) show $z = 0$ cross sections (contour plots) of the gain profiles $-{\rm Im}\epsilon_g$ obtained during the first and final (fixed-point) iteration of the algorithm at two separate radii $R = \{2,2.5\}(c/\omega_{21})$, with black/white denoting min , max $-[{\rm Im}\,\epsilon_g] \approx \{1.9,1.3\}$ and $\{1.9,1.5\}$, respectively. Insets in (b) show the angular radiation intensities $\Phi(\theta)$ at selected radii (black dots), normalized by the maximum intensity $\Phi_{\rm max}$. (c) Φ at a fixed radius $R = 2(c/\omega_{21})$ as a function of $\mathcal{P}/\gamma_{21}^0$, with insets illustrating the evolution of Φ as a function of iteration at a fixed $\mathcal{P}/\gamma_{21}^0 = 10^{-4}$ and for two different values of quantum yields (QY) (see text). All plots compare quantities in the presence (solid blue lines) or absence (dashed black lines) of PE, and under a uniform-medium approximation (UMA) (solid red lines) described in the text; the solid green line in (a) denotes the average Purcell factor $\langle\mathcal{F}\rangle = \frac{1}{V}\int_V \mathcal{F}$ at each radius.

demonstrate the iterative process at a fixed $R = 2(c/\omega_{21})$ and for two different sets of concentrations $n = \{1,5\} \times 10^{19}\,{\rm cm}^{-3}$ and quantum yields $\approx\{10,50\}\%$.

Figure 4 illustrates the impact of PE on the emission of the sphere, showing variation in (a) SE flux $\Phi(\omega_{21})$ and (b) gain directivity Φ_G/Φ of the sphere with respect to radius R at a fixed $\mathcal{P}/\gamma_{21}^0 = 10^{-4}$, or with respect to (c) pump rate $\mathcal{P}$ at a fixed $R = 2(c/\omega_{21})$, both including (solid blue lines) and excluding (dashed black lines) PE. As before, Φ is normalized by $\Phi_{\rm BB}$. Shown as insets in Fig. 4(a) are $z = 0$ cross sections of ${\rm Im}\,\epsilon_g$ for the first and final (fixed-point) iteration of the algorithm, at two different radii $R = \{2,2.5\}(c/\omega_{21})$ (black dots), demonstrating large gain enhancement and spatial variations. As expected, Φ is either enhanced or suppressed depending on the average PE (green line) which we have defined as $\langle\mathcal{F}\rangle \neq 1$, where for convenience we have defined

$$\langle\mathcal{F}\rangle = \frac{1}{V}\int_V \mathcal{F} = \frac{1}{N}\sum_n \Phi_{b_n}/\Phi^0$$
$$= -\frac{1}{2N\Phi^0}{\rm Tr}\, W^* {\rm sym}\, GW.$$

(As discussed above, $\langle\mathcal{F}\rangle \sim \Phi$ turns out to be the Frobenius norm of a low-rank matrix and is therefore susceptible to fast computations.) As shown, at small $R \lesssim 1.2(c/\omega_{21})$, or in the absence of resonances, $\langle\mathcal{F}\rangle < 1$ and hence Φ is suppressed with respect to predictions that neglect PE. Conversely, $\langle\mathcal{F}\rangle > 1$ near resonances and hence Φ is enhanced. Note that for our choice of parameters, the gain profile scales linearly with the quantum yield, i.e., $\epsilon_g \propto {\rm QY} = \gamma_{21}^r/\gamma_{21}$, such that in the limit as $\langle\mathcal{F}\rangle \to \infty$ (ignoring quenching occurring as $\gamma_{21}^r \to \gamma_{10}$), $-{\rm Im}\,\epsilon_g \to 2$. (For smaller QY $\ll 1$, ϵ_g can be many times larger than the bare permittivity with increasing $\langle\mathcal{F}\rangle$, saturating at much larger values of PE.) In addition to changing the overall SE rate, PE also modifies the sphere's directivity. This is illustrated in Fig. 4(b), which shows enhancements in Φ_G/Φ and correspondingly changes in emission patterns (insets) at selective $R = \{2,2.5\}(c/\omega_{21})$.

Figure 4(c) also explores the dependence of Φ on $\mathcal{P}$ at a fixed $R = 2(c/\omega_{21})$, showing that Φ peaks at a finite value of $\mathcal{P}/\gamma_{12}^0 \gtrsim 10^{-4}$ and then decreases with increasing $\mathcal{P}$; the same is true for $\langle\mathcal{F}\rangle$ and $\langle\epsilon_g\rangle$ (not shown). Such a nonmonotonicity stems from the fact that near the critical pump rate, ${\rm Im}\,\epsilon_g \approx {\rm Re}\,\epsilon_g$, causing the resonance frequency to shift to smaller radii, a trend that is observed both in the presence and absence of PE. Surprisingly, however, we find that while PE causes large inhomogeneities in ϵ_g, in both scenarios the peak emission is approximately the same, suggesting the possibility that one could explain the impact of PE by a simple UMA. In what follows, we exploit a UMA that not only greatly simplifies the calculation of PE but also leads to accurate results over a wider range of parameters. In particular, we consider a UMA in which the otherwise inhomogeneous gain profile of the object is replaced with that of a uniform medium $\epsilon_g(\mathbf{x}) \to \langle\epsilon_g\rangle$ (assuming a uniform pump rate) given by (1) but with $\gamma_{21}^r \to \langle\gamma_{21}^r\rangle = \langle\mathcal{F}\rangle\gamma_{21}^{r,0}$, corresponding to a homogeneous broadening/narrowing of the gain atoms throughout the sphere. Within this approximation, the system of nonlinear equations above is described by a single (as opposed to $N \gg 1$) degree of freedom $\langle\gamma_{21}^r\rangle$, enabling faster convergence and application of algorithms especially suited for handling low-dimensional systems of equations [99]. Ignoring other sources of inhomogeneity (e.g., induced by density or pump variations), such an approximation allows calculation of Φ via scattering formulations best suited for handling piecewise-constant dielectrics, including SIE [100] and related scattering matrix [76] methods. The solid red lines in Fig. 4 are obtained by employing the UMA, demonstrating its validity over a wide range of parameters. Surprisingly, we find that this holds even in regimes marked by strong gain saturation (e.g., $\gamma_{10} \lesssim \gamma_{21}$). It follows that in this geometry, the effect of PE on radiation can be attributed primarily to the presence of a larger average gain or pump

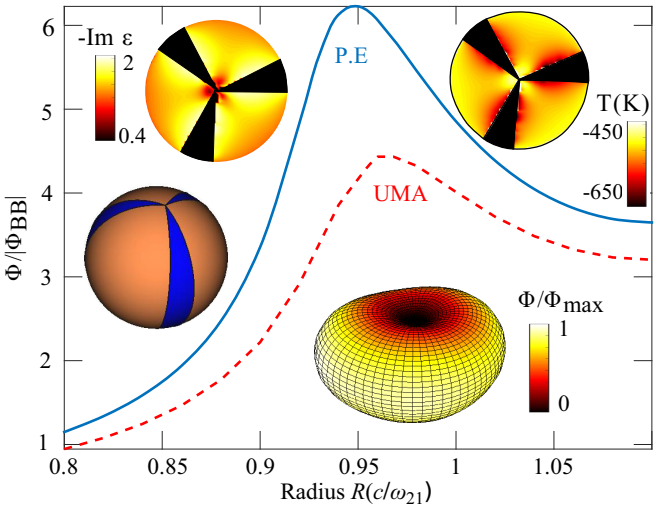

FIG. 5. Self-consistent treatment of Purcell effect (PE) in the metal-dielectric composite shown on the inset, with orange and blue denoting Er^{3+}-doped polymer and Au regions, described via full solution of (1) and (8) (solid blue lines) or via the uniform-medium approximation (dashed red line) described in the text. The solid line shows the SE flux Φ from the particle as a function of radius R (in units of c/ω_{21}). Insets show $z = 0$ cross sections of the gain profile $-\mathrm{Im}\epsilon_g$ (top) and active temperature (right), along with the angular radiation intensity $\Phi(\theta,\phi)$ (bottom) at a selected $R = 0.95(c/\omega_{21})$, normalized by the maximum intensity $\Phi_{\max}$.

rate in the sphere, whereas the actual spatial variation in ϵ_g is largely unimportant.

There are geometries and situations where such a UMA is expected to fail, e.g., structures subject to even large dielectric inhomogeneities (as in Fig. 3). Such conditions arise in large objects (supporting higher-order resonances) or in metal-dielectric composites (supporting highly localized surface waves). Figure 5 shows Φ for one such structure (bottom inset): a dielectric sphere with the same gain medium (orange) of Fig. 4 but partitioned into three metallic (red) regions along the azithmutal direction, given by $\epsilon(\phi) = -2 + i$ for $\phi \in [2n\pi/3, 2n\pi/3 + \pi/8]$, where $n = 0,1,2$. (Note that our choice of ϵ for the metal does not lead to a strong plasmonic resonance, but still yields significant subwavelength confinement.) A $z = 0$ cross section of the steady state ϵ_g and temperature distributions at a fixed $R = 0.95c/\omega_{21}$ are shown on the top inset, demonstrating significant and complex variations in both quantities. In particular, while population inversion is suppressed near the metal (black regions), ε_g attains its maximum value (white regions) close to the metal surface, decaying rapidly within the dielectric. Comparing the exact (solid blue lines) and UMA (dashed red line) predictions, one finds that the presence of multiple nodes in ϵ_g leads to a dramatic failure for UMA (with a peak error of $\approx$50%). Despite the different radiation rates, however, we find that UMA effectively captures the main features of the far-field radiation pattern (inset).

IV. CONCLUDING REMARKS

We have shown that wavelength-scale, active-composite bodies can lead to complex radiative effects, depending sensitively on the arrangement of gain and loss. By exploiting a general-purpose formulation of EM fluctuations, we quantified the non-negligible impact that dielectric and noise inhomogeneities can have on emission in these systems. Furthermore, we introduced an approach that captures feedback from Purcell effect (i.e., the optical environment) on the gain medium. We note that in situations where ASE is dominated by relatively few leaky resonances, it is possible and practical to perform a similar procedure by expanding the fields in terms of eigenmodes, in which case the problem boils down to solution of a linear generalized eigenvalue problem for the leaky modes. (In VIE as in FDFD or related brute-force methods, leaky modes can be computed via the solution of a generalized eigenvalue problem of the form $Z(\omega)\xi = 0$, for a complex frequency [101].) However, the FVC approach above is advantageous in that it casts the problem in the context of solutions of relatively few ($\ll$ degrees of freedom) scattering calculations. More importantly, FVC can handle structures supporting many modes or situations where near-field effects are of interest and contribute to PE [68]. The latter is especially important when the relevant quantity is the energy exchange between two nearby objects, a regime that motivated initial development of these and related scattering methods [67]. Note that above we mainly explored structures with small $\mathrm{Re}\,\epsilon \approx 4$ and large gain concentration n, leading to large $\mathrm{Im}\,\epsilon_g \lesssim \mathrm{Re}\,\epsilon$ even for relatively weakly confined resonances. However, similar effects can be obtained with smaller n and $\mathrm{Im}\,\epsilon_g$ in structures with larger $\mathrm{Re}\,\epsilon$ and dimensions, or supporting highly localized fields (e.g., spacers), where there exists larger Purcell enhancement. Finally, we note that micron-scale particles like the spheres explored above lie within the reach of current experiments [102].

ACKNOWLEDGMENTS

We would like to thank Li Ge, Hakan Tureci, Steven G. Johnson, Zin Lin, and Jacob Khurgin for useful discussions. This work was partially supported by the Army Research Office through the Institute for Soldier Nanotechnologies under Contract No. W911NF-13-D-0001 and by the National Science Foundation under Grant No. DMR-1454836.

[1] M. Premaratne and G. P. Agrawal, *Light Propagation in Gain Media: Optical Amplifiers* (Cambridge University Press, Cambridge, UK, 2011).

[2] L. Allen, in *Coherence and Quantum Optics*, edited by L. Mandel and E. Wolf (Springer, New York, 1973), pp. 467–490.

[3] R. H. Dicke, Phys. Rev. **93**, 99 (1954).
[4] F. Lahoz, C. J. Oton, D. López, J. Marrero-Alonso, A. Boto, and M. Díaz, Org. Electron. **14**, 1225 (2013).
[5] L. Allen and G. Peters, Phys. Rev. A **8**, 2031 (1973).
[6] C. R. Giles and E. Desurvire, J. Lightwave Technol. **9**, 271 (1991).
[7] R. Gutiérrez-Castrejón and M. Duelk, IEEE J. Quantum Electron. **42**, 581 (2006).
[8] P. Wang and W. Clarkson, Opt. Lett. **32**, 2605 (2007).
[9] G. Yoo, H.-S. Sim, and H. Schomerus, Phys. Rev. A **84**, 063833 (2011).
[10] L. Ge and A. D. Stone, Phys. Rev. X **4**, 031011 (2014).
[11] Y. D. Chong, L. Ge, H. Cao, and A. D. Stone, Phys. Rev. Lett. **105**, 053901 (2010).
[12] A. Polimeridis, J. Villena, L. Daniel, and J. White, J. Comput. Phys. **269**, 280 (2014).
[13] A. G. Polimeridis, M. Reid, S. G. Johnson, J. K. White, and A. W. Rodriguez, IEEE Trans. Antennas Propag. **63**, 611 (2015).
[14] A. G. Polimeridis, M. T. H. Reid, W. Jin, S. G. Johnson, J. K. White, and A. W. Rodriguezz, Phys. Rev. B **92**, 134202 (2015).
[15] W. Jin, A. G. Polimeridis, and A. W. Rodriguez, Phys. Rev. B **93**, 121403(R) (2016).
[16] D. J. Bergman and M. I. Stockman, Phys. Rev. Lett. **90**, 027402 (2003).
[17] M. I. Stockman, Phys. Rev. Lett. **106**, 156802 (2011).
[18] M. I. Stockman, in *Active Plasmonics and Tuneable Plasmonic Metamaterials*, edited by A. V. Zayats and S. A. Maier (Wiley, Hoboken, NJ, 2013).
[19] H. Iwase, D. Englund, and J. Vučković, Opt. Express **18**, 16546 (2010).
[20] Q. Gu, B. Slutsky, F. Vallini, J. S. Smalley, M. P. Nezhad, N. C. Frateschi, and Y. Fainman, Opt. Express **21**, 15603 (2013).
[21] A. Cerjan, Y. Chong, and A. D. Stone, Opt. Express **23**, 6455 (2015).
[22] V. M. Parfenyev and S. S. Vergeles, Phys. Rev. A **86**, 043824 (2012).
[23] N. Arnold, B. Ding, C. Hrelescu, and T. A. Klar, Beilstein J. Nanotechnol. **4**, 974 (2013).
[24] O. Zaitsev and L. Deych, J. Opt. **12**, 024001 (2010).
[25] J. Andreasen and H. Cao, Phys. Rev. A **82**, 063835 (2010).
[26] N. Bachelard, J. Andreasen, S. Gigan, and P. Sebbah, Phys. Rev. Lett. **109**, 033903 (2012).
[27] S. F. Liew, B. Redding, L. Ge, G. S. Solomon, and H. Cao, Appl. Phys. Lett. **104**, 231108 (2014).
[28] L. Ge, O. Malik, and H. E. Türeci, Nat. Photon. **8**, 871 (2014).
[29] X. Fan, Z. Shen, and B. Luk'yanchuk, Opt. Express **18**, 24868 (2010).
[30] V. V. Prosentsov, Physical Science International Journal **8**, 1 (2015).
[31] W. Heiss, J. Phys. A **45**, 444016 (2012).
[32] Z. Lin, H. Ramezani, T. Eichelkraut, T. Kottos, H. Cao, and D. N. Christodoulides, Phys. Rev. Lett. **106**, 213901 (2011).
[33] L. Ge, Y. D. Chong, and A. D. Stone, Phys. Rev. A **85**, 023802 (2012).
[34] H. Alaeian and J. A. Dionne, Phys. Rev. A **89**, 033829 (2014).
[35] M. Kulishov and B. Kress, Opt. Express **21**, 22327 (2013).
[36] Y. D. Chong, L. Ge, and A. D. Stone, Phys. Rev. Lett. **106**, 093902 (2011).
[37] S. Longhi and L. Feng, Opt. Lett. **39**, 5026 (2014).
[38] M.-A. Miri, M. A. Eftekhar, M. Facao, and D. N. Christodoulides, in *CLEO: QELS_Fundamental Science* (Optical Society of America, New York, 2014), pp. FM1D–5.
[39] E.-M. Graefe and H. F. Jones, Phys. Rev. A **84**, 013818 (2011).
[40] M. Turduev, M. Botey, R. Herrero, I. Giden, H. Kurt, and K. Staliunas, in *Photonics Conference (IPC), 2014 IEEE* (IEEE, New York, 2014), pp. 164–165.
[41] L. Feng, Z. J. Wong, R.-M. Ma, Y. Wang, and X. Zhang, Science **346**, 972 (2014).
[42] B. Peng, Ş. K. Özdemir, F. Lei, F. Monifi, M. Gianfreda, G. L. Long, S. Fan, F. Nori, C. M. Bender, and L. Yang, Nat. Phys. **10**, 394 (2014).
[43] H. Haken, *Light* (North-Holland, Amsterdam, 1985).
[44] A. E. Siegman, *Lasers* (University Science Books, New York, 1986).
[45] W. Zhou, M. Dridi, J. Y. Suh, C. H. Kim, D. T. Co, M. R. Wasielewski, G. C. Schatz, T. W. Odom *et al.*, Nat. Nanotechnol. **8**, 506 (2013).
[46] J. Andreasen and H. Cao, Opt. Express **19**, 3418 (2011).
[47] A. Cerjan, Y. Chong, L. Ge, and A. D. Stone, Opt. Express **20**, 474 (2012).
[48] S. Esterhazy, D. Liu, M. Liertzer, A. Cerjan, L. Ge, K. G. Makris, A. D. Stone, J. M. Melenk, S. G. Johnson, and S. Rotter, Phys. Rev. A **90**, 023816 (2014).
[49] O. Hess, J. Pendry, S. Maier, R. Oulton, J. Hamm, and K. Tsakmakidis, Nat. Mater. **11**, 573 (2012).
[50] R. Buschlinger, M. Lorke, and U. Peschel, Phys. Rev. B **91**, 045203 (2015).
[51] A. Pusch, S. Wuestner, J. M. Hamm, K. L. Tsakmakidis, and O. Hess, ACS Nano **6**, 2420 (2012).
[52] P. Bermel, E. Lidorikis, Y. Fink, and J. D. Joannopoulos, Phys. Rev. B **73**, 165125 (2006).
[53] A. Cerjan, A. Pick, Y. D. Chong, S. G. Johnson, and A. D. Stone, Opt. Express **23**, 28316 (2015).
[54] A. Cerjan and A. D. Stone, Phys. Scr. **91**, 013003 (2015).
[55] G. J. de Valcárcel, E. Roldán, and F. Prati, Rev. Mex. Fis. E **52**, 198 (2006).
[56] S. Burkhardt, M. Liertzer, D. O. Krimer, and S. Rotter, Phys. Rev. A **92**, 013847 (2015).
[57] P. Hénon, P. Ramet, and J. Roman, Parallel Comput. **28**, 301 (2002).
[58] P. Guillaume, SIAM J. Matrix Anal. Appl. **20**, 575 (1999).
[59] H. E. Türeci, A. D. Stone, and B. Collier, Phys. Rev. A **74**, 043822 (2006).
[60] J. Andreasen and H. Cao, J. Lightwave Technol. **27**, 4530 (2009).
[61] S. Campione, M. Albani, and F. Capolino, Opt. Mater. Express **1**, 1077 (2011).
[62] S.-L. Chua, Y. Chong, A. D. Stone, M. Soljačić, and J. Bravo-Abad, Opt. Express **19**, 1539 (2011).
[63] K. Yasumoto, *Electromagnetic Theory and Applications for Photonic Crystals* (CRC Press, Boca Raton, FL, 2005).
[64] E. K. Lau, R. S. Tucker, and M. C. Wu, *Conference on Lasers and Electro-Optics* (Optical Society of America, New York, 2008), p. CTuGG5.
[65] A. Taflove, S. C. Hagness *et al.*, *Norwood*, 2nd ed. (Artech House, Boston, 1995).
[66] W. C. Chew, E. Michielssen, J. Song, and J. Jin, *Fast and Efficient Algorithms in Computational Electromagnetics* (Artech House, Inc., Boston, 2001).

[67] X. Liu, L. Wang, and Z. M. Zhang, Nanoscale Microscale Thermophys. Eng. **19**, 98 (2015).
[68] C. Khandekar, W. Jin, O. D. Miller, A. Pick, and A. W. Rodriguez, arXiv:1511.04492 (2015).
[69] S. Strauf and F. Jahnke, Laser Photon. Rev. **5**, 607 (2011).
[70] N. Gregersen, T. Suhr, M. Lorke, and J. Mork, Appl. Phys. Lett. **100**, 131107 (2012).
[71] R. Matloob, R. Loudon, M. Artoni, S. M. Barnett, and J. Jeffers, Phys. Rev. A **55**, 1623 (1997).
[72] J. R. Jeffers, N. Imoto, and R. Loudon, Phys. Rev. A **47**, 3346 (1993).
[73] R. Graham and H. Haken, Z. Phys. **213**, 420 (1968).
[74] A. Pick, A. Cerjan, D. Liu, A. W. Rodriguez, A. D. Stone, Y. D. Chong, and S. G. Johnson, Phys. Rev. A **91**, 063806 (2015).
[75] M. Patra and C. W. J. Beenakker, Phys. Rev. A **60**, 4059 (1999).
[76] G. Bimonte, Phys. Rev. A **80**, 042102 (2009).
[77] R. Messina and M. Antezza, Phys. Rev. A **84**, 042102 (2011).
[78] J. D. Jackson, *Classical Electrodynamics*, 3rd ed. (Wiley, New York, 1998).
[79] A. Hochman, J. Fernandez Villena, A. G. Polimeridis, L. M. Silveira, J. K. White, and L. Daniel, IEEE Trans. Antennas Propag. **62**, 3150 (2014).
[80] W. Chai and D. Jiao, IEEE Trans. Components, Packaging Manufacturing Technol. **3**, 2113 (2013).
[81] E. Waks and D. Sridharan, Phys. Rev. A **82**, 043845 (2010).
[82] X. Wu, T. Ming, X. Wang, P. Wang, J. Wang, and J. Chen, ACS Nano **4**, 113 (2009).
[83] Y. Fang, W.-S. Chang, B. Willingham, P. Swanglap, S. Dominguez-Medina, and S. Link, ACS Nano **6**, 7177 (2012).
[84] D. Lu, J. J. Kan, E. E. Fullerton, and Z. Liu, Nat. Nanotechnol. **9**, 48 (2014).
[85] P. T. Kristensen, J. E. Mortensen, P. Lodahl, and S. Stobbe, Phys. Rev. B **88**, 205308 (2013).
[86] E. Süli and D. F. Mayers, *An Introduction to Numerical Analysis* (Cambridge University Press, Cambridge, UK, 2003).
[87] H. Voss, BIT Numer. Math. **44**, 387 (2004).
[88] H. F. Walker and F.-P. Iteration, WPI Math. Sciences Dept. Report No. MS-6-15-50, 2011, http://users.wpi.edu/∼walker/Papers/anderson_accn_algs_imps.pdf.
[89] H. Ramachandran, Pramana **58**, 313 (2002).
[90] H. Zhu, X. Chen, L. M. Jin, Q. J. Wang, F. Wang, and S. F. Yu, ACS Nano **7**, 11420 (2013).
[91] J. A. Harrington, *Infrared Fibers and Their Applications* (SPIE Press, Bellingham, WA, 2004).
[92] G. Zhang, H. Zhang, X. Zhang, S. Zhu, L. Zhang, Q. Meng, M. Wang, Y. Li, and B. Yang, J. Mater. Chem. **22**, 21218 (2012).
[93] E. K. Macdonald and M. P. Shaver, Polym. Int. **64**, 6 (2015).
[94] P. G. Eliseev and V. Van Luc, Pure Appl. Opt.: J. Eur. Opt. Soc. A **4**, 295 (1995).
[95] J. A. Lock, JOSA A **18**, 3085 (2001).
[96] Y.-H. Chen, J. Li, M.-L. Ren, and Z.-Y. Li, Small **8**, 1355 (2012).
[97] G. Grynberg, A. Aspect, and C. Fabre, *Introduction to Quantum Optics: From the Semi-classical Approach to Quantized Light* (Cambridge University Press, Cambridge, UK, 2010).
[98] A. Godard, C. R. Phys. **8**, 1100 (2007).
[99] A. R. Conn, K. Scheinberg, and L. N. Vicente, *Introduction to Derivative-free Optimization* (SIAM, New York, 2009), Vol. 8.
[100] A. W. Rodriguez, M. T. H. Reid, and S. G. Johnson, Phys. Rev. B **86**, 220302(R) (2012).
[101] N. Marcuvitz, IRE Trans. Antennas Propag. **4**, 192 (1956).
[102] J. J. Kaufman, G. Tao, S. Shabahang, E.-H. Banaei, D. S. Deng, X. Liang, S. G. Johnson, Y. Fink, and A. F. Abouraddy, Nature (London) **487**, 463 (2012).